Paving “Pt···Ti” Hot Electron Transportation Bridge for Outstanding Photothermal Catalytic Reduction of CO2

Jiang, Peng; Liu, Wen-Rui; Wang, Kun; Ding, Yang; Wang, Chun-Hua; Hau Ng, Yun; Chen, Li-Hua; Su, Bao Lian

Published in:
CCS Chemistry

DOI:
10.31635/ccschem.024.202404469

Publication date:
2024

Document Version
Publisher's PDF, also known as Version of record

CCS Chemistry

RESEARCH ARTICLE

Received: May 13, 2024 | Accepted: Aug. 19, 2024 | Published: Oct. 8, 2024

Paving "Pt · · · Ti" Hot Electron Transportation Bridge for Outstanding Photothermal Catalytic Reduction of CO_2

Peng Jiang[1], Wen-Rui Liu[1], Kun Wang[1], Yang Ding[2]*, Chun-Hua Wang[3], Yun Hau Ng[3], Li-Hua Chen[1]* & Bao-Lian Su[1,4]*

[1]*State Key Laboratory of Advanced Technology for Materials Synthesis and Processing, Wuhan University of Technology, Wuhan 430070,* [2]*College of Materials and Environmental Engineering, Hangzhou Dianzi University, Hangzhou 310018,* [3]*School of Energy and Environment, City University of Hong Kong, Kowloon 999077, Hong Kong,* [4]*Laboratory of Inorganic Materials Chemistry (CMI), University of Namur, B-5000 Namur*

**Corresponding authors: dingyang@hdu.edu.cn; chenlihua@whut.edu.cn; bao-lian.su@unamur.be*

Cite this: *CCS Chem*. **2024**, Just Published. DOI: 10.31635/ccschem.024.202404469

Coupling photocatalysis with thermocatalysis is considered the best way for CO_2 reduction to produce useful hydrocarbons. Particularly, photocatalytic CO_2 reduction activity could be improved via the photothermal effect induced by local heat and subsequently, enhance visible light harvesting from noble metal nanoparticles. However, the sluggish hot electron transfer between noble metal and semiconducting materials remains an Achilles heel to achieve an applicable CO_2 reduction. Herein, a highly efficient "Pt · · · Ti" hot electron transportation bridge between Pt nanoparticles and hierarchically porous TiO_2 (HP-TiO_2) was paved. Such photothermocatalyst lowered the barrier of charge migration and exhibited significantly boosted CO_2 reduction with an outstanding hydrocarbon productivity of 29.68 $\mu mol \cdot h^{-1} \cdot g^{-1}$, which was around 21 times higher than that of bulk-TiO_2; besides, an extraordinary selectivity to CH_4 of over 99% under simulated sunlight irradiation was achieved. In-situ characterizations and first-principle calculations confirmed that the manufactured "Pt · · · Ti" hot electron transportation bridge exerted a significant role in promoting CO_2 molecule activation and conversion. The innovative concept of paving an efficient hot electron shift bridge, acting as a crucial springboard promises a practical application of advanced photothermocatalyst for efficient industrial CO_2 reduction and high-valued chemical production.

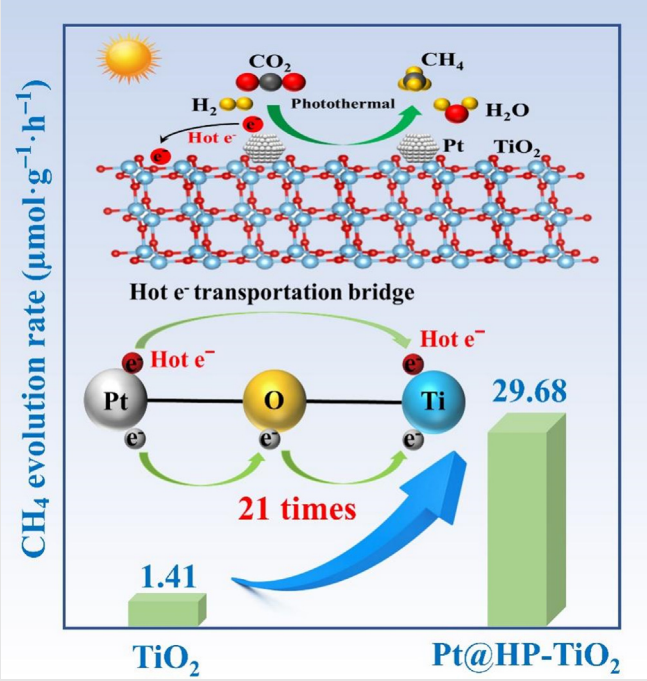

Keywords: photocatalytic CO_2 reduction, photothermal effect, Pt nanoparticle, hierarchically porous TiO_2, hydrocarbon production

Citation: *CCS Chem*. **2024**, Just Published. DOI: 10.31635/ccschem.024.202404469
Link to VoR: https://doi.org/10.31635/ccschem.024.202404469

Introduction

Photocatalysis using solar energy combined with the additional driving force provided by the thermal effect could be highly beneficial to enhance CO_2 reduction and value-added product generation. Compared with the thermocatalytic process consuming considerable energy, the photothermal catalysis induced by the photothermal effect is considered one of the best technologies to convert solar energy to chemical energy.[1–10] Gold, platinum, silver, palladium, and other noble metal particles are widely used in photocatalytic reactions owing to their strong visible light absorption and harvesting.[11–13] Noble metal particles can not only prohibit the photogenerated electron-hole pairs recombination but also lead to efficient surface charge migration. Notably, the photothermal effect of noble metal particles arises from the excitation of hot electrons and the rapid thermal relaxation of excitons, resulting in the rapid conversion of solar energy to heat. Coupling semiconductors with noble metal to form a Schottky junction is quite promising for photothermal catalytic CO_2 reduction.[14]

TiO_2 is widely used in photocatalytic CO_2 reduction because of its nontoxicity, excellent stability, high light response, and low-cost characteristics.[15–19] However, its wide bandgap, narrow light response range, and fast recombination of photogenerated electron-hole pairs impede the photocatalytic CO_2 reduction activity. The three-dimensionally ordered macroporous (3DOM) structure with a large specific surface area has been shown to provide more active sites for photocatalytic reactions.[20–24] Thus, 3DOM TiO_2 is a preferred material to enhance light absorption and improve photocatalytic CO_2 reduction. Pt nanoparticles can be coupled with TiO_2 for efficient photocatalytic CO_2 reduction via photothermal effect owing to their strong visible light absorption, improved charge separation, increased local temperature of the active site, facilitated CO_2 adsorption and activation, and low surface reaction energy. Although there are some reports for photocatalytic CO_2 reduction,[14] the photothermal catalytic activity is still far away from practical applications; efficient hot electron transfer between noble metal and photocatalytic semiconductor materials remains highly challenging, severely restricting CO_2 reduction.

Herein, we have fabricated a highly efficient "Pt · · · Ti" hot electron transportation bridge, innovatively built between Pt nanoparticles and hierarchically porous TiO_2 (HP-TiO_2) for exceptional photothermal reduction of CO_2 to CH_4. The loading of Pt nanoparticles on HP-TiO_2 increased the temperature of the reaction environment via hot electrons induced by photothermal effect while the hierarchically porous structure of Pt@HP-TiO_2 provided convenient mass diffusion channels and abundant active sites. In-situ characterizations and first-principle calculations demonstrated that the created "Pt · · · Ti" hot electron transportation bridge exerted a crucial effect in promoting CO_2 molecule activation and conversion. As a result, the prepared Pt@HP-TiO_2 photothermocatalyst presented an extraordinary CH_4 evolution rate of 29.68 $\mu mol \cdot h^{-1} \cdot g^{-1}$, being about 21 times higher than that of bulk-TiO_2, with a selectivity higher than 99% under simulated sunlight irradiation. The heat transfer and hot electron shift between Pt and HP-TiO_2 were thoroughly investigated. The paving of an efficient "Pt · · · Ti" hot electron shift bridge served as a novel perspective in designing advanced photothermal catalysts for efficient CO_2 reduction and high-valued chemical production.

Experimental Methods

Materials

Styrene (C_8H_8, AR), titanium tetraisopropanolate (TTIP, $C_{12}H_{28}O_4Ti$, 98%) and potassium persulfate ($K_2S_2O_8$, AR) were obtained from Sinopharm Chemical Reagent Co., Ltd. (Shanghai, China) Chloroplatinic acid hexahydrate ($H_2PtCl_6 \cdot 6H_2O$, AR) was purchased from Aladdin Industrial Co. Ltd. (Shanghai, China).

Synthesis of Pt@HP-TiO_2

The preparation of polystyrene (PS) template was a prerequisite condition and depicted as follows: 47 g of styrene and 400 mL of deionized water were added to a three-necked flask and stirred for 30 min under a nitrogen atmosphere. The mixture in a three-necked flask was heated to 80 °C, then 0.43 g of $K_2S_2O_8$ was added and reacted for 6 h to obtain a PS emulsion with a particle size of 500 nm. Finally, the PS template was obtained by drying the PS emulsion at 60 °C.

The detailed synthetic process of Pt@HP-TiO_2 is illustrated in Supporting Information Figure S1: Briefly, TTIP was added into the PS template in the three-necked flask so that the PS template was filled with TTIP. Then the TTIP@PS was allowed to age for 24 h at room temperature. Next, the aged TTIP@PS was heated at 550 °C for 4 h at a heating rate of 2 °C/min in a muffle furnace to remove the PS template. HP-TiO_2 was obtained after cooling down to room temperature naturally. Platinum nanoparticles loaded with hierarchically porous TiO_2 (Pt@HP-TiO_2) were prepared by photodeposition of Pt nanoparticles onto the synthesized HP-TiO_2. Specifically, 500 mg HP-TiO_2 was added to 5 mL H_2PtCl_6 solution (1 mg/mL), then irradiated under 365 nm UV light with stirring for 2 h. Finally, Pt@HP-TiO_2 was obtained after the mixture dried in air at 60 °C for 24 h. Pt nanoparticles loaded bulk-TiO_2 (Pt@B-TiO_2) composite was prepared in the same way as above without the PS template.

Citation: *CCS Chem.* **2024**, Just Published. DOI: 10.31635/ccschem.024.202404469
Link to VoR: https://doi.org/10.31635/ccschem.024.202404469

Characterization

The microstructures were observed by scanning electron microscopy (SEM; Hitachi S-4800, Tokyo, Japan) and transmission electron microscopy (TEM; Talos F200S, Waltham, Massachusetts, USA). The X-ray powder diffraction (XRD) patterns were obtained using an X-ray diffraction machine (Bruker D8 Advance, Karlsruhe, Germany) using Cu Kα (λ = 0.15418 nm) radiation. The X-ray photoelectron spectroscopy (XPS; Omicron Sphera II, Taunusstein, Germany) data was tested on a monochromated Al Kα X-ray source (hv = 1486.6 eV) at 15 kV/150 W to detect the chemical states of elements in the samples. Nitrogen adsorption isotherms, pore size distribution curve, and Brunauer–Emmett–Teller (BET) surface area were obtained on a nitrogen adsorption apparatus (TriStar II 2020, Norcross, USA). The UV–vis diffuse reflectance spectra (UV–vis DRS) were performed by UV–VIS-NIR spectrometer (Lambda 750S, PerkinElmer, Waltham, Massachusetts, USA) over a range of 200–800 nm. Infrared thermographys were taken by Infrared Thermal Camera (UTi260B, Dongguan, China). In-situ kelvin probe force microscopy (KPFM) image and the surface potential were tested by MFP-3D Infinity (Oxford Instruments, Oxford, UK). Electrochemical impedance spectra (EIS), transient photocurrent spectra, and the Mott–Schottky (M–S) curve were acquired using an electrochemical workstation (CS2350H, CorrTest, Wuhan, Hubei, China) in 0.5 M Na_2SO_4 solution at room temperature using a 300W Xenon lamp (PLS-167 SXE300, Beijing PerfectLight, Beijing, China). The Pt plate and Ag/AgCl were applied as the counter electrode and the reference electrode, respectively. The photoluminescence spectra (PL) and time-resolved PL spectra were performed on a Fluoromax-4 spectrophotometer (FL-3, HORIBA Scientific, Kyoto, Japan) with 375 nm as the excitation wavelength, and decay curves were fitted using bi-exponential decay function to obtain deconvolution of the instrument response function. In-situ time-resolved diffuse reflectance infrared Fourier transform (DRIFT) spectra were obtained using a Fourier transform infrared spectrometer (VERTEX V80, Bruker, Karlsruhe, Germany). Finite-difference time-domain (FDTD) simulation and density functional theory (DFT) calculation details are given in Supporting Information. In FDTD simulations, the illumination direction of the light source was parallel to the Z axis and perpendicular to the XY plane. The wavelength ranges of UV light and visible light were 200–400 nm and 400–800 nm, respectively.

Photocatalytic CO_2 reduction

In a typical photocatalytic experiment, 100 mg of catalyst was placed on the stainless steel mesh of a 200 mL stainless steel reactor with an optical quartz window at the top. The reactor was first vacuumed, and then CO_2 and H_2 were introduced into the reactor at a volume ratio of 1:4 for half an hour to blow out the air in the reactor. A 300 W Xenon lamp (PLS-SXE300, Beijing PerfectLight) with a filter (AM 1.5 G, Ceaulight Technology Co. Ltd., China) was used to simulate solar illumination with about 100 $mW \cdot cm^{-2}$. The reactor was irradiated with a Xenon lamp for the desired time. During the photocatalytic reaction process, the gaseous mixture was periodically sampled from the stainless steel reactor every 0.5 h and analyzed by gas chromatography (GC-9790II; Fuli Analytical Instruments).

Results and Discussion

Microstructure and physical properties analysis

Figures 1a,b show the field-emission scanning electron microscopy (FESEM) images of the as-prepared Pt@HP-TiO_2. It was observed that the Pt@HP-TiO_2 displayed a 3DOM structure with a pore diameter of around 500 nm. Meanwhile, the pores communicate with each other, therefore, favorable for mass diffusion. TEM image (Figure 1c) clearly showed that the Pt nanoparticles were uniformly dispersed on the surface of HP-TiO_2, and the corresponding high-resolution TEM (HRTEM) picture suggested that the lattice-fringe spacings of 0.23 and 0.35 nm were indexed into the (111) plane of Pt and (101) plane of TiO_2 (Figure 1d), respectively. Furthermore, the high-angle annular dark-field (HAADF) picture (Supporting Information Figure S2a) and its corresponding elemental mapping images (Supporting Information Figure S2b–d) demonstrated a uniform distribution of Ti, O, and Pt elements in Pt@HP-TiO_2 composite. FESEM images of bulk-TiO_2 (B-TiO_2), Pt@B-TiO_2, HP-TiO_2 and PS template are shown in the Supporting Information Figures S3–S6 as the references. XRD was employed to identify the phase structures of the obtained samples. As presented in Supporting Information Figure S7, all the peaks of B-TiO_2, HP-TiO_2, Pt@B-TiO_2, and Pt@HP-TiO_2 corresponded to the typical diffraction pattern of anatase TiO_2 (PDF#21–1272).[25] The diffraction peaks of Pt were not observed in both Pt@B-TiO_2 and Pt@HP-TiO_2 samples because of the low content and too small a particle size of Pt.

The textural properties were evaluated via nitrogen adsorption-desorption isotherms. As shown in Supporting Information Figure S8, all the samples displayed typical type IV isotherms, signifying abundant mesoporosity existed in the 3DOM structure. Moreover, BET surface areas (S_{BET}) of the HP-TiO_2 (43 $m^2 \cdot g^{-1}$) and Pt@HP-TiO_2 (51 $m^2 \cdot g^{-1}$) were much larger than those of B-TiO_2 (16 $m^2 \cdot g^{-1}$) and Pt@B-TiO_2 (14 $m^2 \cdot g^{-1}$) (Supporting Information Table S1). The large specific surface areas of the HP-TiO_2 and Pt@HP-TiO_2 supplied abundant surface adsorption and active sites, which were favorable

Citation: *CCS Chem.* **2024**, Just Published. DOI: 10.31635/ccschem.024.202404469
Link to VoR: https://doi.org/10.31635/ccschem.024.202404469

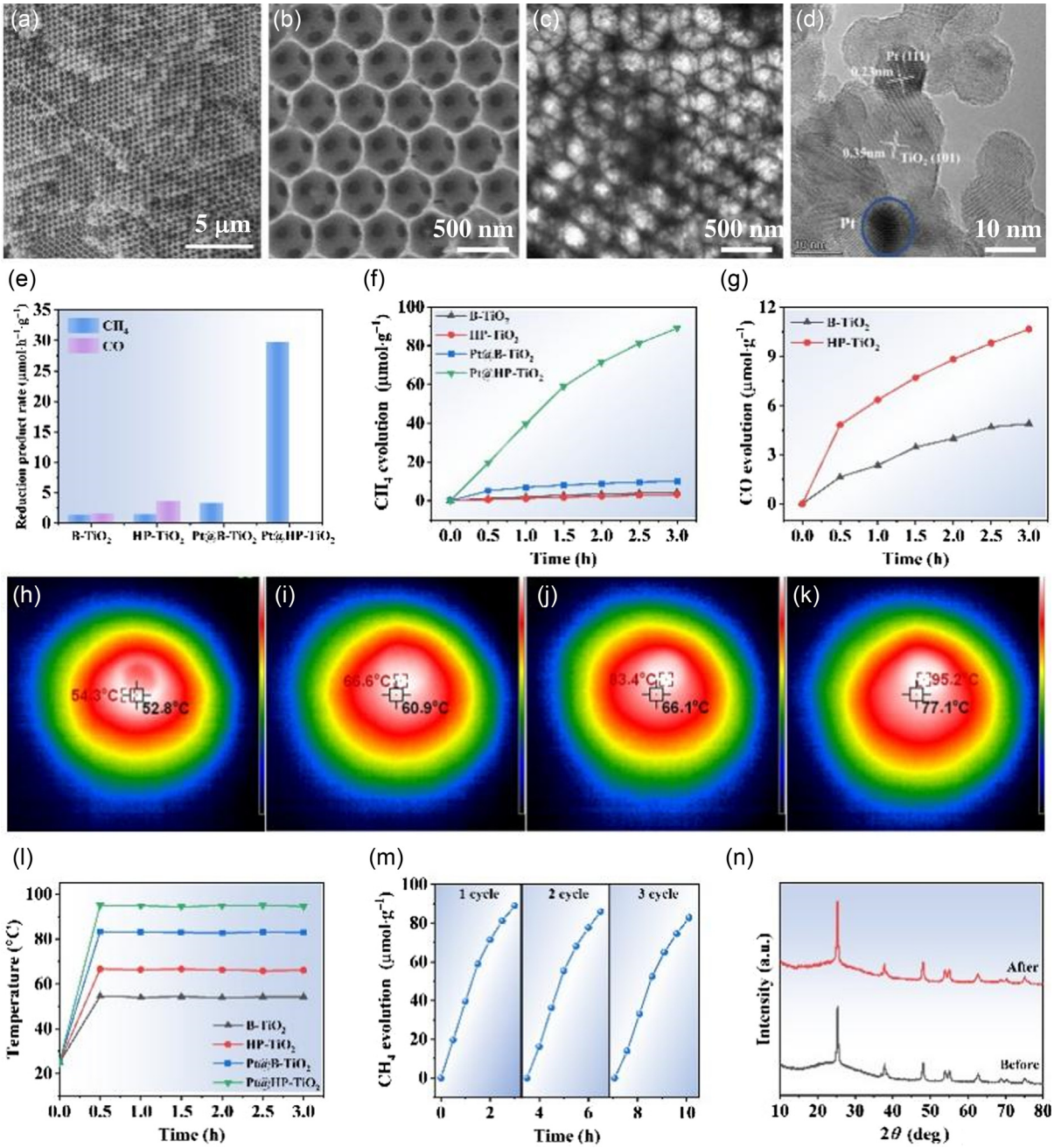

Figure 1 | *(a, b) FESEM images of Pt@HP-TiO_2, (c) TEM and its corresponding (d) HRTEM images of Pt@HP-TiO_2; (e) Products evolution rate via photocatalytic CO_2 reaction, (f) time-dependent CH_4 evolution, (g) time-dependent CO evolution; infrared thermographies of (h) B-TiO_2, (i) HP-TiO_2, (j) Pt@B-TiO_2 and (k) Pt@HP-TiO_2 under Xe lamp irradiation; (l) time-dependent reaction temperatures of B-TiO_2, HP-TiO_2, Pt@B-TiO_2, and Pt@HP-TiO_2; (m) photocatalytic stability test of Pt@HP-TiO_2, (n) XRD patterns before and after the stability tests of Pt@HP-TiO_2.*

for the capture and activation of CO_2. Besides, the large specific surface area of the HP-TiO_2 offered more loading sites to disperse Pt nanoparticles for further enhanced photocatalytic ability. From the pore size distribution curves in Supporting Information Figure S9, we found that HP-TiO_2 and Pt@HP-TiO_2 showed obvious meso-pores centered at 3.5 nm in comparison with B-TiO_2 and Pt@B-TiO_2. The meso-macro porous structure in Pt@HP-TiO_2 was very favorable for facile mass diffusion and transfer.

Since light absorption efficiency was directly related to the photocatalytic performance of the catalyst, UV–vis DRS were recorded to investigate the photoresponse properties of the as-prepared samples. As shown in Supporting Information Figure S10, the strong light ab-sorption properties of B-TiO_2, HP-TiO_2, Pt@B-TiO_2, and

Citation: *CCS Chem.* **2024**, Just Published. DOI: 10.31635/ccschem.024.202404469
Link to VoR: https://doi.org/10.31635/ccschem.024.202404469

Pt@HP-TiO_2 were observed within the range of 200–400 nm. In particular, HP-TiO_2 and Pt@HP-TiO_2 have stronger light absorption performance than that of B-TiO_2 and Pt@B-TiO_2. Compared with B-TiO_2 and HP-TiO_2, Pt@B-TiO_2 and Pt@HP-TiO_2 performed increased light adsorption properties in the range of 400–800 nm (visible light region) because of the visual light absorption of Pt nanoparticles.

Conversion of CO_2 via photothermal effect

The photothermal catalytic CO_2 reduction of different samples was evaluated. As depicted in Figure 1e, CO and CH_4 were the major photoreduction products for B-TiO_2 and HP-TiO_2, while CH_4 was the only photoreduction product of Pt@B-TiO_2 and Pt@HP-TiO_2. The production evolution rates of Pt@HP-TiO_2 and HP-TiO_2 were higher than those of T Pt@B-TiO_2 and B-TiO_2, respectively, indicating the 3DOM structured TiO_2 provided more reaction active sites for the photothermal catalytic CO_2 reduction. The selectivities of CH_4 evolution over Pt@B-TiO_2 and Pt@HP-TiO_2 were much higher than 99%. Compared with B-TiO_2 and HP-TiO_2, the product evolution rates of Pt@B-TiO_2 and Pt@HP-TiO_2 were higher, especially for the CH_4 productivity over Pt@HP-TiO_2. The CH_4 evolution rate over Pt@HP-TiO_2 increased by ~21, 20.5, and 9 times compared with that of B-TiO_2, HP-TiO_2, Pt@B-TiO_2, respectively, attaining 29.68 $\mu mol \cdot h^{-1} \cdot g^{-1}$. It is worth noting that CO_2 conversion performance over our prepared Pt@HP-TiO_2 was also superior to other TiO_2-based photocatalysts reported in previous publications (Supporting Information Table S2).

The photothermal catalytic CO_2 reduction stability was estimated by long-term consecutive photothermal catalytic reduction measurement and cycled test. The CH_4 yield of Pt@HP-TiO_2 grew nearly linearly with time (Figure 1f) and was much higher than those on other samples during the photocatalytic CO_2 reduction. The CO yield of HP-TiO_2 was higher than that of B-TiO_2 because of the abundant reaction active sites in HP-TiO_2 (Figure 1g). Figure 1h–k show the infrared thermographies of B-TiO_2, HP-TiO_2, Pt@B-TiO_2, and Pt@HP-TiO_2 under Xe lamp irradiation. It was apparent that Pt@HP-TiO_2 gave the higher reacting temperature and the photocatalytic CO_2 reaction temperature distribution on the surfaces of samples was quite uniform. As shown in Figure 1l, the local temperature of the reaction system ranks in the order: Pt@HP-TiO_2>Pt@B-TiO_2>HP-TiO_2>B-TiO_2. The higher reaction temperatures of Pt@B-TiO_2 and Pt@HP-TiO_2 in comparison with those of B-TiO_2 and HP-TiO_2 implied that the Pt nanoparticles induced increased visible light absorption and improved the reacting temperature. Compared with B-TiO_2 and Pt@B-TiO_2, Pt@HP-TiO_2 and HP-TiO_2 showed a higher reacting temperature, implying the 3DOM structured TiO_2 harvests more UV absorbance. Thus, the highest CH_4 evolution yield of Pt@HP-TiO_2 could be related to the photothermal effect ascribed to the synergy between light absorption of Pt and 3DOM structure of TiO_2. The photocatalytic reaction temperatures of all samples remained stable after the photocatalytic CO_2 reduction of 0.5 h. The CH_4 yield of Pt@HP-TiO_2 exhibited only minor changes during the cycled stability test (Figure 1m), indicating its excellent stability during the photocatalytic CO_2 reduction. XRD patterns of Pt@HP-TiO_2 showed no noticeable change before and after the photocatalytic CO_2 reaction (Figure 1n), further suggesting the good stability of the Pt@HP-TiO_2. To explore the impact of reaction temperature on the performance of Pt@HP-TiO_2, the photothermal catalytic CO_2 reduction performances by varying the light intensity are shown in Supporting Information Figure S11a. No production evolved when Ar or H_2 was introduced as the reaction gas. When the light intensities increased to 150 and 200 $mW \cdot cm^{-2}$, the CH_4 evolution rates of Pt@HP-TiO_2 increased to 48.82 and 75.54 $\mu mol \cdot h^{-1} \cdot g^{-1}$, respectively. Meanwhile, as shown in Supporting Information Figure S11b, the reaction temperatures of Pt@HP-TiO_2 increased to 108.5 and 125.0 °C, respectively, which suggested that the stronger light intensity could excite more hot electrons to increase the reaction temperature.

Mechanism of conversion of CO_2 via photothermal effect

The surface element composition and surface chemical state of HP-TiO_2 and Pt@HP-TiO_2 were investigated by XPS, together with the in-situ irradiated XPS under light irradiation. As presented in Supporting Information Figure S12, XPS survey spectra indicate that Ti, O, and Pt elements exist in the Pt@HP-TiO_2, which was in accordance with the energy-dispersive X-ray spectroscopy (EDS) results (Supporting Information Figure S2b–d). As for HP-TiO_2, the peaks centered at 458.5 and 464.2 eV, were assigned to the $2p_{3/2}$ and $2p_{1/2}$ of Ti (Figure 2a), and the peaks centered at 529.4 and 531.4 eV were attributed to the Ti–O bond and surface hydroxyl –OH) group (Figure 2b), respectively. The peaks centered at 70.9, 74.3, 72.9, and 76.3 eV corresponded to Pt^0 $4f_{7/2}$, Pt^0 $4f_{5/2}$, Pt^{2+} $4f_{7/2}$, and Pt^{2+} $4f_{5/2}$ for Pt@HP-TiO_2 (Figure 2c), respectively.[26] The presence of Pt^{2+} was ascribed to the formation of the Pt–O–Ti bond. Changes in binding energy reflect variations in electron density, and the decreased electron density generally resulted in increased binding energy.[19,27,28] The binding energy change was employed to examine the direction of charge carrier transfer in photocatalysts. From Figure 2a, the binding energies of Ti 2p in Pt@HP-TiO_2 shifted toward higher energy levels, indicating a decrease in the electron density of Ti in HP-TiO_2 and the migration of electrons from Ti of HP-TiO_2 to Pt. The binding energies of O 1s in Pt@HP-TiO_2 significantly shifted to lower energy levels

Citation: *CCS Chem.* **2024**, Just Published. DOI: 10.31635/ccschem.024.202404469
Link to VoR: https://doi.org/10.31635/ccschem.024.202404469

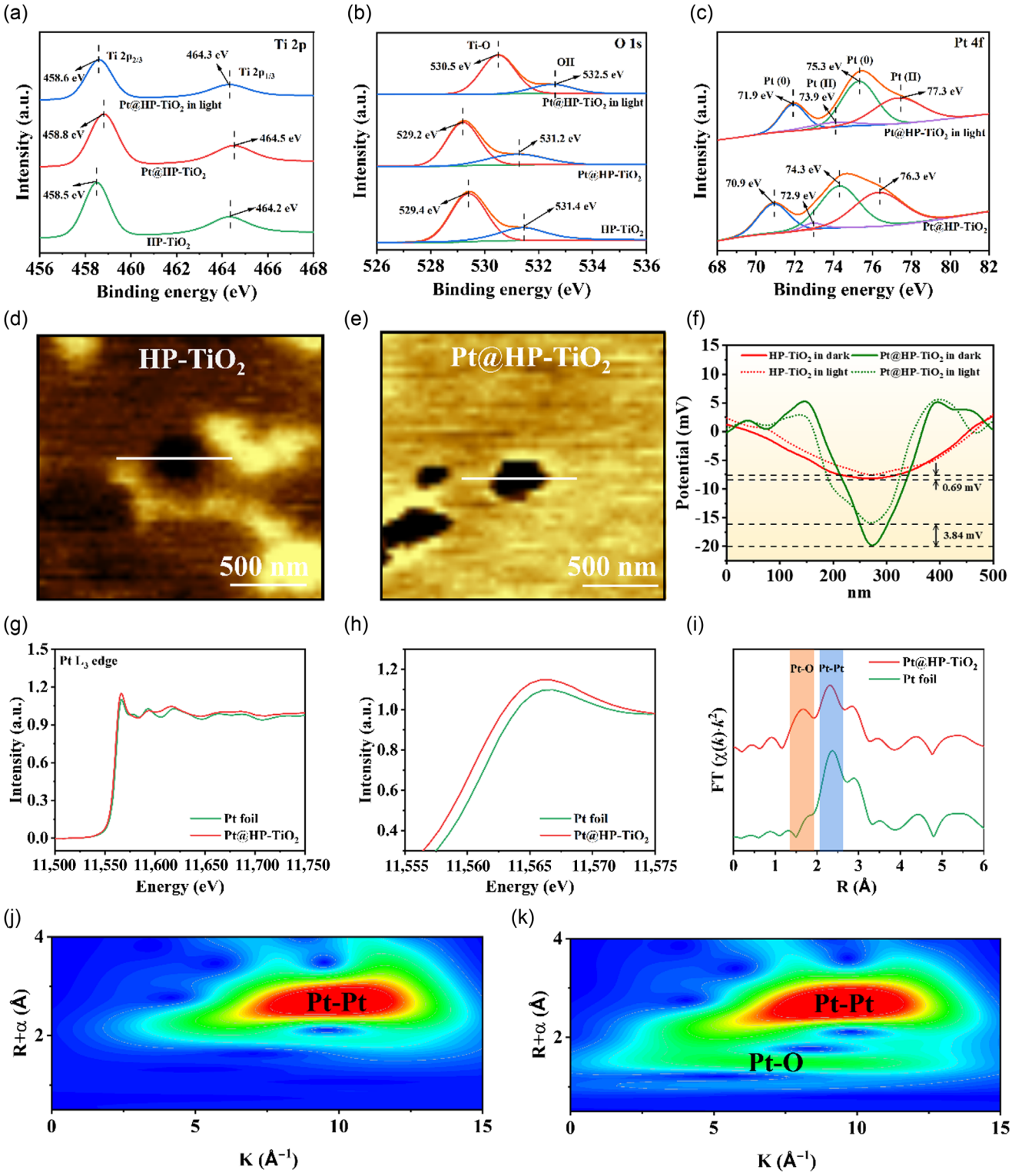

Figure 2 | *In-situ high-resolution XPS spectra of (a) Ti 2p, (b) O 1s, and (c) Pt 4f of HP-TiO_2 and Pt@HP-TiO_2; In-situ KPFM images for (d) HP-TiO_2 and (e) Pt@HP-TiO_2 under light irradiation, (f) surface potential profiles of HP-TiO_2 and Pt@HP-TiO_2 before and after light irradiation; (g, h) Pt L_3-edge XANES spectra and (i) Pt L_3-edge FT EXAFS spectra of the obtained samples; (j, k) WT EXAFS images of the obtained samples.*

Citation: *CCS Chem.* **2024**, Just Published. DOI: 10.31635/ccschem.024.202404469
Link to VoR: https://doi.org/10.31635/ccschem.024.202404469

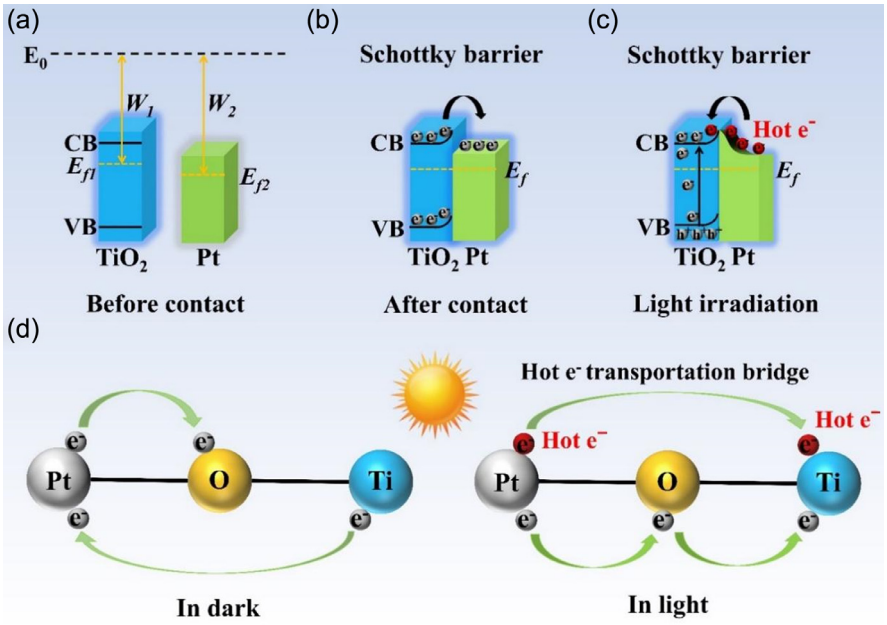

Figure 3 | *Schematic illustrations of the electron transfer mechanism between TiO_2 and Pt (a) before contact, (b) after contact, and (c) after contact under light irradiation; (d) Schematic diagram of "Pt · · · Ti" hot electron transportation bridge.*

(Figure 2b), assigning to the electron transfer from Pt^0 to O^{2-} due to the strong metal (Pt)-support (TiO_2) interaction (SMSI).[29] However, based on the in-situ XPS under light irradiation, the binding energies of Ti 2p in the Pt@HP-TiO_2 markedly move to a lower energy level (Figure 2a). Meanwhile, the binding energies of Pt^0 $4f_{7/2}$, Pt^0 $4f_{5/2}$, Pt^{2+} $4f_{7/2}$, and Pt^{2+} $4f_{5/2}$ in Pt@HP-TiO_2 shifted to higher energy levels under light irradiation (Figure 2c), thus implying that the hot electrons migrate from Pt to HP-TiO_2. Therefore, these XPS results provided important evidence that the "Pt · · · Ti" electron transportation bridge was paved on the interface between Pt nanoparticles and HP-TiO_2. Compared with Pt@HP-TiO_2 in the dark, the binding energies of O 1s in Pt@HP-TiO_2 significantly moved to higher energy levels under light irradiation (Figure 2b), indicating that the photogenerated electrons migrated from O to Ti. Both the hot electrons migrated from Pt to Ti via the "Pt · · · Ti" bridge and the photogenerated electrons from O to Ti were very favorable for efficient electron migration and improved photothermal reduction of CO_2. The difference in work functions (W) or Fermi levels (E_f) for HP-TiO_2 and Pt was the internal driving force of charge transfer in photocatalytic CO_2 reduction. To verify the charge migration route, in-situ KPFM coupled with an external Xe light source was adopted to record the potential distribution change of HP-TiO_2 and Pt@HP-TiO_2 (Figure 2d,e). As shown in Figure 2f, the surface potential difference of HP-TiO_2 before and after illumination is 0.69 mV, indicating that the photogenerated electrons of HP-TiO_2 were transferred to the surface of the catalyst. The surface potential of Pt@HP-TiO_2 was lower than that of HP-TiO_2 before illumination, illustrating that electrons were transferred from HP-TiO_2 to Pt. The surface potential difference of Pt@HP-TiO_2 before and after illumination was 3.84 mV, indicating that more electrons were gathered on the surface of Pt@HP-TiO_2. Under light irradiation, not only the photogenerated electrons migrated to the surface of HP-TiO_2 but the hot electrons were also transferred from Pt to HP-TiO_2 via the efficient "Pt · · · Ti" hot electron transportation bridge.[30,31] The in-situ KPFM results were in excellent agreement with the observation by in-situ XPS.

The X-ray absorption near-edge spectroscopy (XANES) spectra of Pt L_3-edge were performed to study the local structural variation of Pt species in Pt@HP-TiO_2. From normalized XANES curves of Pt L_3-edge, the absorption edge energy and white-line intensity of Pt@HP-TiO_2 were higher than those of Pt foil (Figure 2g,h). The results revealed the presence of electronic Pt–TiO_2 interactions on Pt@HP-TiO_2, which further indicated that charge transfer occurred between Pt nanoparticles and O atoms. As shown in Figure 2i, Pt–Pt and Pt–O bonds present in the Fourier-transformed extended X-ray absorption fine structure (FT EXAFS) spectrum of Pt@HP-TiO_2, while only Pt–Pt bond presents in that of Pt foil.[32–34] As shown in Figure 2j, the wavelet transform EXAFS (WT EXAFS) image of Pt foil only displayed maximum intensity at 10.4 $Å^{-1}$, which was the result of the Pt–Pt bond. The WT EXAFS image (Figure 2k) of Pt@HP-TiO_2 showed that the

Citation: *CCS Chem.* **2024**, Just Published. DOI: 10.31635/ccschem.024.202404469
Link to VoR: https://doi.org/10.31635/ccschem.024.202404469

maximum intensity at 7.5 and 10.4 $Å^{-1}$ belonged to the contribution of Pt–O and Pt–Pt bonds, respectively. The above results further solidly indicated that Pt–O bonds existed on Pt@HP-TiO_2, which provided an electron transfer path between Pt-HP-TiO_2 through "Pt · · · Ti".

On account of the results of photoirradiated KPFM and in-situ irradiated XPS, the charge migration route, including hot electrons transportation, photogenerated electrons transfer, and electron migration between Pt and HP-TiO_2 was proposed. As shown in Figure 3a, before TiO_2 contacts Pt, TiO_2 had a smaller work function (W_1) and higher Fermi level (E_{f1}), while Pt had a larger W_2 and lower E_{f2}. When TiO_2 was made contact with Pt, the electrons transferred from TiO_2 to Pt until the E_f at the interface equilibrated (Figure 3b). Concurrently, TiO_2 showed upward interface band bending. followed by a positively charged interface due to the loss of electrons. Consequently, the electron transfer created a Schottky barrier at the interfaces pointing from TiO_2 to Pt. When Pt@HP-TiO_2 was irradiated under sunlight, the electrons were excited from the valence band to the conduction band (VB to CB) of TiO_2; at the same time, hot electrons were generated on the Pt. Hot electrons could overstep the Schottky barrier and transfer from Pt to CB of TiO_2 at the interface because they possess higher energy than those of normally excited electrons (Figure 3c). Upon irradiation, more electrons were excited from VB to CB for photocatalytic CO_2 reduction, and more holes were generated at the VB for oxidizing H_2 to *H. The hot electrons from Pt increased the reaction temperature of the photocatalytic CO_2 reduction. Such a process could reduce the recombination rate of photogenerated electron-hole pairs and increase their availability for CO_2 photoreduction, thus highly enhanced by hot electrons induced by the photothermal effect. Specifically, the electron transfer routes of Pt@HP-TiO_2 in the dark and light are shown in Figure 3d. In the dark, the electrons transferred from Pt to O through the "Pt–O" bond due to strong metal (Pt)-support (TiO_2) interaction. Meanwhile, the electrons in Ti migrated to Pt due to the difference in work function and Fermi level. Upon irradiation of Pt@HP-TiO_2, the hot electrons overstepped the Schottky barrier and were transferred from Pt to Ti via the efficient "Pt · · · Ti" hot electron transportation bridge, thereby exciting the photogenerated electrons from O to Ti.

The photocatalytic CO_2 reduction activity was closely related to the photogenerated charge carriers separation and transfer, the PL and photoelectrochemical characterizations were, thus, performed to unravel the charge dynamics of the samples. As displayed in Supporting Information Figure S13a, compared with B-TiO_2 and HP-TiO_2, the steady-state PL intensities of Pt@B-TiO_2 and Pt@HP-TiO_2 were lower, implying that the construction of the Schottky barrier between Pt and TiO_2 effectively inhibited the recombination of photogenerated charge carriers. The lower steady-state PL intensities of HP-TiO_2 and Pt@HP-TiO_2 in comparison with B-TiO_2 and Pt@B-TiO_2 indicated that the 3DOM structure was helpful for the separation of photogenerated charges. The PL peaks of HP-TiO_2, Pt@B-TiO_2, and Pt@HP-TiO_2 displayed apparent blueshift in comparison with B-TiO_2, indicating that the recombination of photogenerated electron-hole pairs was suppressed and the formation of the heterostructure. These results firmly demonstrated that both co-decoration of Pt nanoparticles and 3DOM structure efficiently reduced the recombination of photogenerated electron-hole pairs, being consistent with the highest photocatalytic CO_2 reduction activity of Pt@HP-TiO_2. Moreover, the average PL lifetime (τ_{ave}) of Pt@HP-TiO_2 (0.71 ns) was shorter than those of B-TiO_2 (0.86 ns), Pt@B-TiO_2 (0.76 ns), and HP-TiO_2 (0.74 ns), further indicating a more efficient separation and transfer of photogenerated carriers (Supporting Information Figure S12b). EIS spectra and transient photocurrent spectra were measured to deeply reveal the charge separation and transport behaviors of the photocatalysts. As shown in Supporting Information Figure S12c,d, Pt@HP-TiO_2 displayed the smallest EIS radius and higher photocurrent density than those of B-TiO_2, HP-TiO_2, Pt@B-TiO_2, reaffirming its highly efficient photogenerated charge carriers separation and transfer, which corresponded to the PL results.

To study the effect of Pt on the TiO_2 electronic state and the electron transport mechanism on Pt–O bridge in photothermal catalytic CO_2 reduction, a DFT calculation model for density of states (DOS) and charge difference of Pt–O electron transport bridge was established based on the EXAFS results of Pt–O coordination. The DOS for anatase (101) and Pt-loaded anatase (101), as well as the charge density difference for Pt-loaded anatase (101), were calculated by DFT (Supporting Information Figure S14). As shown in Figure 4a, the valence band of pure TiO_2 was mainly composed of O 2p and Ti 3d states, while its conduction band primarily consisted of Ti 3d states. No spin polarization was observed as the spin-up states and spin-down states were symmetric. After Pt loading onto the TiO_2 (101) surface, new states above the valence band appeared, as shown in Figure 4b. The Pt acted as an electron capture center, which caused new states in the DOS and the shift of the Femi level.[35,36] The new states of DOS indicated the construction of the Pt–O bond, which facilitated the transport of electrons from TiO_2 to Pt. The electron capture center could be demonstrated by the charge density difference. The interfacial charge transfer calculation (Figure 4c) undoubtedly confirmed Pt as an electron capture center, as Pt attracted electrons from TiO_2. This would be beneficial for photocatalytic CO_2 reduction via photothermal effect since Pt was able to generate more hot electrons under light irradiation. To better figure out the changes in electromagnetic field intensity caused by the photothermal effect, 3D-FDTD simulations were performed to reveal the spatial

Citation: *CCS Chem.* **2024**, Just Published. DOI: 10.31635/ccschem.024.202404469
Link to VoR: https://doi.org/10.31635/ccschem.024.202404469

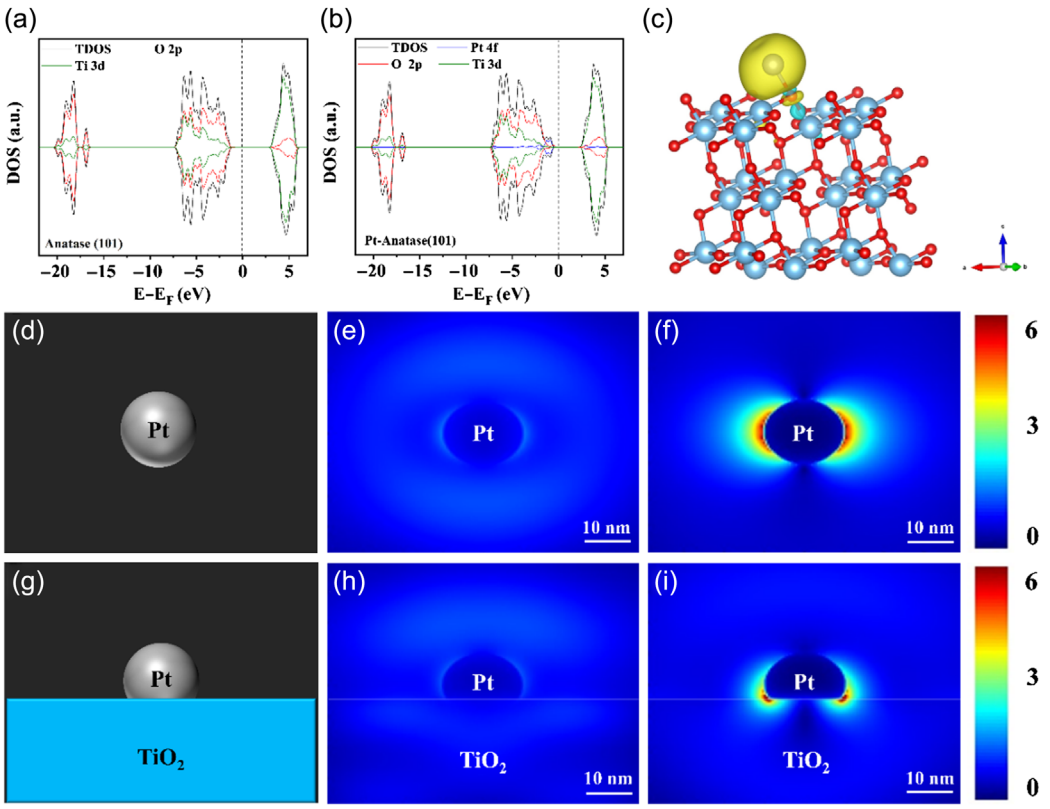

Figure 4 | *DOS for (a) pure anatase (101), (b) Pt loaded anatase (101) by DFT calculation, and (c) charge density difference for Pt loaded anatase (101) (Yellow: electron gain, Blue: electron loss). FDTD simulations models for (d) Pt nanoparticle and (g) Pt nanoparticle loaded TiO_2; spatial electromagnetic field for (e) Pt nanoparticle and (h) Pt nanoparticle loaded TiO_2 under UV light excitation from the FDTD simulations; spatial electromagnetic field for (f) Pt nanoparticle and (i) Pt nanoparticle loaded TiO_2 under visual light excitation from the FDTD simulations.*

electromagnetic field distributions. The models of Pt nanoparticle and Pt nanoparticle loaded TiO_2 are shown in Figure 4d,g. The spatial electromagnetic field of the Pt nanoparticle and the Pt nanoparticle-loaded TiO_2 were performed under UV light and visible light irradiation, respectively. As shown in Figure 4e,h, the electromagnetic field intensity of the Pt nanoparticle was low, and there was no strong interfacial electromagnetic field between the Pt nanoparticle and TiO_2 under an excitation wavelength of 200–400 nm. There was no hot electron generation and injection in the Pt nanoparticle-loaded TiO_2 under UV light irradiation. While under 400–800 nm light excitation the strong electromagnetic field of the Pt nanoparticle (Figure 4f) indicated the hot electrons generation on the surface of the Pt nanoparticle. The strong electromagnetic field emerged at the interface between the Pt nanoparticle and TiO_2 (Figure 4i), which demonstrated energy transfer from the Pt nanoparticle to TiO_2. The hot electrons were generated on the Pt nanoparticle and transferred from the Pt nanoparticle to TiO_2 under visible light irradiation. The FDTD simulation results were consistent with the experiments and characterization conclusions.

To clarify the photocatalytic CO_2 reduction mechanism and charge transfer pathway over Pt@HP-TiO_2 induced by the photothermal effect, an in-situ diffuse reflectance infrared Fourier transform spectroscopy (DRIFTS) was performed to unveil possible reaction intermediates involved in the photocatalytic CO_2 reduction reaction. The in-situ DRIFTS spectra of Pt@HP-TiO_2 were collected in the dark and under light irradiation conditions as a comparison (Figure 5a). Without introducing CO_2 and H_2 gas in the dark (0 min), no absorption peaks were detected. When CO_2 and H_2 gas were introduced in the dark (5–15 min), monodentate carbonate species (m-CO_3^{2-}, 1453, 1486, and 1554 cm^{-1}), bidentate carbonate species (b-CO_3^{2-}, 1281, 1317, 1525, 1580, and 1653 cm^{-1}) and carbon dioxide (CO_2, 2292–2411 cm^{-1}) were detected.[37–41] These peaks indicates that CO_2 was effectively adsorbed and activated on the surface of Pt@HP-TiO_2. Besides, some new peaks were observed under light irradiation (5–30 min). The new emerging peaks were attributed to carboxylate species (COO^-, 1343 and 1363 cm^{-1}), formaldehyde species ($HCHO^-$, 1507 and 1773 cm^{-1}), and methoxy groups (CH_3O^-, 1694, 1714, and 1745 cm^{-1}).[37,39,40] The intensity of carbon dioxide (CO_2, 2292–2411 cm^{-1})

Citation: *CCS Chem.* **2024**, Just Published. DOI: 10.31635/ccschem.024.202404469
Link to VoR: https://doi.org/10.31635/ccschem.024.202404469

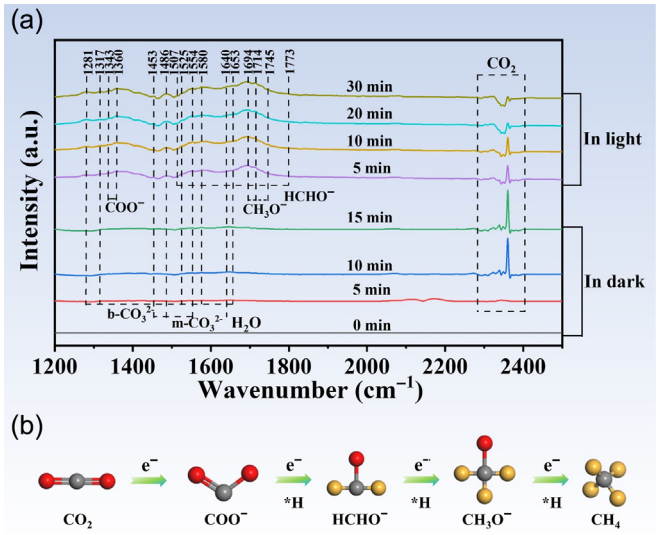

Figure 5 | *(a) In-situ DRIFTS spectra of Pt@HP-TiO_2. (b) Possible photocatalytic CO_2 reduction reaction pathways on the surface of Pt@HP-TiO_2.*

decreased gradually with increasing reaction time under irradiation, which suggested that the CO_2 was progressively reduced. We deduced that COO^-, $HCHO^-$, and CH_3O^- acted as the essential intermediate species during photocatalytic CO_2 reduction on Pt@HP-TiO_2. Compared with HP-TiO_2, Pt@HP-TiO_2 adsorb more CO intermediate to prohibit the formation of CO because of the strong adsorption ability between the CO intermediate and Pt nanoparticles.[42-44] The formation of CO from the CO intermediate was a quick reaction process in the photocatalytic CO_2 reduction, and the strong interaction of Pt and CO intermediate prohibited the CO intermediate from capturing electrons to form CO, thereby further propelling the generation of CH_4. Thus, a possible photocatalytic CO_2 reduction mechanism and pathway driven by photothermal effect over Pt@HP-TiO_2 was established, as follows: First, CO_2 and H_2 were adsorbed on the surface of Pt@HP-TiO_2. The photogenerated electrons excited from VB to CB of TiO_2 and hot electrons were generated on the Pt under simulated sunlight irradiation. Hot electrons could overstep the Schottky barrier and transfer from Pt to CB of TiO_2 at the interface simultaneously, such that more photogenerated electrons were excited from VB to CB of TiO_2 and more holes were generated at VB upon light irradiation. Subsequently, the H_2 molecule was oxidized into an H atom (*H) by photoinduced holes, and the CO_2 molecule obtained photogenerated electrons to form COO^- species. Afterward, COO^- reacted with *H and photogenerated electrons to produce $HCHO^-$ species. Then the $HCHO^-$ gained *H and photogenerated electrons to form CH_3O^- species. Finally, CH_3O^- was hydrogenated to form CH_4. Therefore, as shown in Figure 5b, the proposed pathway for photocatalytic CO_2 reduction over Pt@HP-TiO_2 spurred by photothermal effect could be briefly expressed as follows: $CO_2 \rightarrow COO^- \rightarrow HCHO^- \rightarrow CH_3O^- \rightarrow CH_4$. Thus, the high selectivity of CO_2 conversion into CH_4 on the Pt@HP-TiO_2 catalyst induced by the photothermal effect was reliable and excellent.

Conclusion

An innovative "Pt · · · Ti" hot electron transportation bridge was paved on the interface between Pt nanoparticles and HP-TiO_2 by constructing Pt@HP-TiO_2 composite for outstanding photothermal reduction of CO_2. Pt@HP-TiO_2 exhibited superior photocatalytic CO_2 reduction with a CH_4 evolution rate of 29.68 $\mu mol \cdot h^{-1} \cdot g^{-1}$ and a higher selectivity of >99% under simulated sunlight irradiation, which was about 21 times higher than that of bulk-TiO_2. Compared with previous 3DOM structured and noble metal nanoparticles loaded photocatalysts with only structure or light-harvesting merit in photocatalytic process, the efficient "Pt · · · Ti" hot electron transportation bridge innovatively engineered in our HP-TiO_2 photothermocatalyst exerted the most significant role in promoting photoreduction of CO_2, and the photocatalytic CO_2 reduction potential was further exploited in noble metal/3DOM semiconductor system, thus leading to outstanding CH_4 production rate. We envisioned that paving an efficient hot electron shift bridge could act as a crucial springboard in exploring advanced photothermal catalysts for more efficient CO_2 and high-valued chemical evolution.

Supporting Information

Supporting Information is available and includes FDTD simulation and DFT calculation details, Figures S1–S14, and Tables S1–S2.

Conflict of Interest

There is no conflict of interest to report.

Acknowledgments

This work was supported by the National Key R&D Program of China (grant no. 2022YFB3504000), the National Natural Science Foundation of China (grant nos. U20A20122, 22402044, 22293022, and U22B6011), and the Zhejiang Provincial Natural Science Foundation of China (grant no. LQ24E020011), the Program of Introducing Talents of Discipline to Universities-Plan 111 (grant no. B20002) from the Ministry of Science and Technology and the Ministry of Education of China. This work was also supported by the European Commission Interreg V France-Wallonie-Vlaanderen project "DepollutAir," the

Program Win2Wal (TCHARBONACTIF: 2110120), the Wallonia Region of Belgium and the National Key R&D Program Intergovernmental Technological Innovation Special Cooperation Project Wallonia- Belgium-China, Ministry of Science and Technology (MOST) (grant no. SUB/2021/IND493971/524448).

References

1. Hoyt, D. V. An Empirical Determination of the Heating of the Earth by the Carbon Dioxide Greenhouse Effect. *Nature* **1979**, *282*, 388–390.
2. Jiang, X.; Chen, R.; Chen, Y.-X.; Lu, C.-Z. Research Progress of Photoelectrochemical Conversion of CO_2 to C_{2+} Products. *Chem. Synth.* **2024**, *4*, 46.
3. Hansen, J.; Johnson, D.; Lacis, A.; Lebedeff, S.; Lee, P.; Rind, D.; Russell, G. Climate Impact of Increasing Atmospheric Carbon Dioxide. *Science* **1981**, *213*, 957–966.
4. Tian, H.; Lu, C.; Ciais, P.; Michalak, A. M.; Canadell, J. G.; Saikawa, E.; Huntzinger, D. N.; Gurney, K. R.; Sitch, S.; Zhang, B. The Terrestrial Biosphere as a Net Source of Greenhouse Gases to the Atmosphere. *Nature* **2016**, *531*, 225.
5. Li, Y.; Zhang, D.; Qiao, W.; Xiang, H.; Besenbacher, F.; Li, Y.; Su, R. Nanostructured Heterogeneous Photocatalyst Materials for Green Synthesis of Valuable Chemicals. *Chem. Synth.* **2022**, *2*, 9.
6. Beckman, E. J. Sustainable Chemistry Putting Carbon Dioxide to Work. *Nature* **2016**, *531*, 180–181.
7. Yin, Y.; Kang X.; Han, B. Two-Dimensional Materials: Synthesis and Applications in the Electro-Reduction of Carbon Dioxide. *Chem. Synth.* **2022**, *2*, 19.
8. He, J.; Janaky, C. Recent Advances in Solar-Driven Carbon Dioxide Conversion: Expectations Versus Reality. *ACS Energy Lett.* **2020**, *5*, 1996–2014.
9. Izumi, Y. Recent Advances in the Photocatalytic Conversion of Carbon Dioxide to Fuels with Water and/or Hydrogen Using Solar Energy and Beyond. *Coordin. Chem. Rev.* **2013**, *257*, 171–186.
10. Lee, D. K.; Choi, J. I.; Lee, G. H.; Kim, Y.-H.; Kang, J. K. Energy States of a Core-Shell Metal Oxide Photocatalyst Enabling Visible Light Absorption and Utilization in Solar-to-Fuel Conversion of Carbon Dioxide. *Adv. Energy. Mater.* **2016**, *6*, 1600583.
11. Peng, X.; Chen, L.; Liu, Y.; Liu, C.; Huang, H.; Fan, J.; Xiong, P.; Zhu, J. Strain Engineering of Two-Dimensional Materials for Energy Storage and Conversion Applications. *Chem. Synth.* **2023**, *3*, 46.
12. Yu, X.; Yu, Z.; Zhao, H.; Gates, ID.; Hu, J. Photothermal Catalytic H_2 Production over Hierarchical Porous $CaTiO_3$ with Plasmonic Gold Nanoparticles. *Chem. Synth.* **2023**, *3*, 3.
13. Zheng, Y.; Zhang, L.; Guan, J.; Qian, S.; Zhang, Z.; Ngaw, C. K.; Wan, S.; Wang, S.; Lin, J.; Wang, Y. Controlled Synthesis of CuO/Cu_2O for Efficient Photothermal Catalytic Conversion of CO_2 and H_2O. *ACS Sustain. Chem. Eng.* **2021**, *9*, 1754–1761.
14. Zhang, N.; Han, C.; Fu, X.; Xu, Y.-J. Function-Oriented Engineering of Metal-Based Nanohybrids for Photoredox Catalysis: Exerting Plasmonic Effect and Beyond. *Chem* **2018**, *4*, 1832–1861.
15. Huang, C.-Y.; Guo, R.-T.; Pan, W.-G.; Tang, J.-Y.; Zhou, W.-G.; Qin, H.; Liu, X.-Y.; Jia, P.-Y. Eu-Doped TiO_2 Nanoparticles with Enhanced Activity for CO_2 Phpotcatalytic Reduction. *J. CO_2 Util.* **2018**, *26*, 487–495.
16. Meng, A.; Cheng, B.; Tan, H.; Fan, J.; Su, C.; Yu, J. TiO_2/Polydopamine S-Scheme Heterojunction Photocatalyst with Enhanced CO_2 Reduction Selectivity. *Appl. Catal. B-Environ.* **2021**, *289*, 120039.
17. Noeiaghaei, T.; Yun, J.-H.; Nam, S. W.; Zoh, K. D.; Gomes, V. G.; Kim, J. O.; Chae, S. R. The Influence of Geometrical Characteristics on the Photocatalytic Activity of TiO_2 Nanotube Arrays for Degradation of Refractory Organic Pollutants in Wastewater. *Water Sci. Technol.* **2015**, *71*, 1301–1309.
18. Wang, L.; Cheng, B.; Zhang, L.; Yu, J. In Situ Irradiated XPS Investigation on S-Scheme TiO_2@$ZnIn_2S_4$ Photocatalyst for Efficient Photocatalytic CO_2 Reduction. *Small* **2021**, *17*, e2103447.
19. Wang, L.; Zhu, B.; Cheng, B.; Zhang, J.; Zhang, L.; Yu, J. In-Situ Preparation of TiO_2/N-Doped Graphene Hollow Sphere Photocatalyst with Enhanced Photocatalytic CO_2 Reduction Performance. *Chinese J. Catal.* **2021**, *42*, 1648–1658.
20. Liu, J.; Jin, J.; Li, Y.; Huang, H.-W.; Wang, C.; Wu, M.; Chen, L.-H.; Su, B.-L. Tracing the Slow Photon Effect in a ZnO Inverse Opal Film for Photocatalytic Activity Enhancement. *J. Mater. Chem. A* **2014**, *2*, 5051–5059.
21. Liu, J.; Zhao, H.; Wu, M.; Van der Schueren, B.; Li, Y.; Deparis, O.; Ye, J.; Ozin, G. A.; Hasan, T.; Su, B.-L. Slow Photons for Photocatalysis and Photovoltaics. *Adv. Mater.* **2017**, *29*, 1605349.
22. Madanu, T. L.; Mouchet, S. R.; Deparis, O.; Liu, J.; Li, Y.; Su, B. L. Tuning and Transferring Slow Photons from TiO_2 Photonic Crystals to $BiVO_4$ Nanoparticles for Unprecedented Visible Light Photocatalysis. *J. Colloid. Interf. Sci.* **2023**, *634*, 290–299.
23. Zhao, H.; Hu, Z.; Liu, J.; Li, Y.; Wu, M.; Van Tendeloo, G.; Su, B.-L. Blue-Edge Slow Photons Promoting Visible-Light Hydrogen Production on Gradient Ternary 3DOM TiO_2-Au-CdS Photonic Crystals. *Nano Energy* **2018**, *47*, 266–274.
24. Zhao, H.; Li, C. F.; Hu, Z. Y.; Liu, J.; Li, Y.; Hu, J.; Van Tendeloo, G.; Chen, L. H.; Su, B. L. Size Effect of Bifunctional Gold in Hierarchical Titanium Oxide-Gold-Cadmium Sulfide with Slow Photon Effect for Unprecedented Visible-Light Hydrogen Production. *J. Colloid. Interf. Sci.* **2021**, *604*, 131–140.
25. Lee, S. S.; Bai, H.; Liu, Z.; Sun, D. D. Green Approach for Photocatalytic Cu(II)-Edta Degradation over TiO_2: Toward Environmental Sustainability. *Environ. Sci. Technol.* **2015**, *49*, 2541–2548.
26. Huo, J.; Yuan, C.; Wang, Y. Nanocomposites of Three-Dimensionally Ordered Porous TiO_2 Decorated with Pt and Reduced Graphene Oxide for the Visible-Light Photocatalytic Degradation of Waterborne Pollutants. *ACS Appl. Nano Mater.* **2019**, *2*, 2713–2724.
27. Wang, C.; Jiang, X.; Wang, Y.; Tang, Y.; Zhou, J.; Fu, G. Recent Advances in Nonmetallic Modulation of Palladium-Based Electrocatalysts. *Chem. Synth.* **2023**, *3*, 8.

Citation: *CCS Chem.* **2024**, Just Published. DOI: 10.31635/ccschem.024.202404469
Link to VoR: https://doi.org/10.31635/ccschem.024.202404469

28. Zhang, P.; Li, Y.; Zhang, Y.; Hou, R.; Zhang, X.; Xue, C.; Wang, S.; Zhu, B.; Li, N.; Shao, G. Photogenerated Electron Transfer Process in Heterojunctions: In Situ Irradiation XPS. *Small Methods* **2020**, *4*, 2000214.
29. Zhang, M.; Liu, Q.; Sun, W.; Sun, K.; Shen, Y.; An, W.; Zhang, L.; Chen, H.; Zou, X. Nanostructured Intermetallics: From Rational Synthesis to Energy Electrocatalysis. *Chem. Synth.* **2023**, *3*, 28.
30. Wang, Y.; Liu, M.; Fan, F.; Li, G.; Duan, J.; Li, Y.; Jiang, G.; Yao, W. Enhanced Full-Spectrum Photocatalytic Activity of 3D Carbon-Coated C_3N_4 Nanowires via Giant Interfacial Electric Field. *Appl. Catal. B-Environ.* **2022**, *318*, 121829.
31. Yue, X.; Cheng, L.; Fan, J.; Xiang, Q. 2D/2D $BiVO_4$/$CsPbBr_3$ S-Scheme Heterojunction for Photocatalytic CO_2 Reduction: Insights into Structure Regulation and Fermi Level Modulation. *Appl. Catal. B-Environ.* **2022**, *304*, 120979.
32. Gorczyca, A.; Moizan, V.; Chizallet, C.; Proux, O.; Del Net, W.; Lahera, E.; Hazemann, J.-L.; Raybaud, P.; Joly, Y. Monitoring Morphology and Hydrogen Coverage of Nanometric Pt/γ-Al_2O_3 Particles by in Situ HERFD–XANES and Quantum Simulations. *Angew. Chem. Int. Ed.* **2014**, *53*, 12426–12429.
33. Singh, J.; Alayon, E. M. C.; Tromp, M.; Safonova, O. V.; Glatzel, P.; Nachtegaal, M.; Frahm, R.; van Bokhoven, J. A. Generating Highly Active Partially Oxidized Platinum During Oxidation of Carbon Monoxide over Pt/Al_2O_3: In Situ, Time-Resolved, and High-Energy-Resolution X-Ray Absorption Spectroscopy. *Angew. Chem. Int. Ed.* **2008**, *47*, 9260–9264.
34. Newton, M. A.; Ferri, D.; Smolentsev, G.; Marchionni, V.; Nachtegaal, M. Kinetic Studies of the Pt Carbonate-Mediated, Room-Temperature Oxidation of Carbon Monoxide by Oxygen over Pt/Al_2O_3 Using Combined, Time-Resolved XAFS, DRIFTS, and Mass Spectrometry. *J. Am. Chem. Soc.* **2016**, *138*, 13930–13940.
35. Fu, L.; Wang, S.; Cai, J.; Huang, H.; Yang, F.; Xie, S. Recent Advances in Platinum-Group-Metal Based Electrocatalysts for Alkaline Hydrogen Oxidation Reaction. *Chem. Synth.* **2024**, *4*, 8.
36. Wang, X.; Rui, Z.; Zeng, Y.; Ji, H.; Du, Z.; Rao, Q. Synergetic Effect of Oxygen Vacancy and Pd Site on the Interaction Between Pd/Anatase TiO_2 (101) and Formaldehyde: A Density Functional Theory Study. *Catal. Today* **2017**, *297*, 151–158.
37. Bie, C.; Zhu, B.; Xu, F.; Zhang, L.; Yu, J. In Situ Grown Monolayer N-Doped Graphene on Cds Hollow Spheres with Seamless Contact for Photocatalytic CO_2 Reduction. *Adv. Mater.* **2019**, *31*, e1902868.
38. Deng, Y.; Wan, C.; Li, C.; Wang, Y.; Mu, X.; Liu, W.; Huang, Y.; Wong, P. K.; Ye, L. Synergy Effect Between Facet and Zero-Valent Copper for Selectivity Photocatalytic Methane Formation from CO_2. *ACS Catal.* **2022**, *12*, 4526–4533.
39. He, F.; Zhu, B.; Cheng, B.; Yu, J.; Ho, W.; Macyk, W. 2D/2D/0D TiO_2/C_3N_4/Ti_3C_2 Mxene Composite S-Scheme Photocatalyst with Enhanced CO_2 Reduction Activity. *Appl. Catal. B-Environ.* **2020**, *272*, 119006.
40. Soodi, S.; Zhang, J.J.; Zhang, J.; Liu, Y.; Lashgari, M.; Zafeiratos, S.; Züttel, A.; Zhao, K.; Luo, W. Selective Electroreduction of CO_2 to C_{2+} Products on Cobalt Decorated Copper Catalysts. *Chem. Synth.* **2024**, *4*, 44.
41. Yin, G.; Huang, X.; Chen, T.; Zhao, W.; Bi, Q.; Xu, J.; Han, Y.; Huang, F. Hydrogenated Blue Titania for Efficient Solar to Chemical Conversions: Preparation, Characterization, and Reaction Mechanism of CO_2 Reduction. *ACS Catal.* **2018**, *8*, 1009–1017.
42. Jiang, D.; Yao, Y.; Li, T.; Wan, G.; Pereira-Hernández, X. I.; Lu, Y.; Tian, J.; Khivantsev, K.; Engelhard, M. H.; Sun, C.; García-Vargas, C. E.; Hoffman, A. S.; Bare, S. R.; Datye, A. K.; Hu, L.; Wang, Y. Tailoring the Local Environment of Platinum in Single-Atom Pt_1/CeO_2 Catalysts for Robust Low-Temperature CO Oxidation. *Angew. Chem. Int. Ed.* **2021**, *60*, 26054–26062.
43. Wang, Y.; Ren, P.; Hu, J.; Tu, Y.; Gong, Z.; Cui, Y.; Zheng, Y.; Chen, M.; Zhang, W.; Ma, C.; Yu, L.; Yang, F.; Wang, Y.; Bao, X.; Deng, D. Electron Penetration Triggering Interface Activity of Pt-Graphene for CO Oxidation at Room Temperature. *Nat. Commun.* **2021**, *12*, 5814.
44. Zhou, Y.; Doronkin, D. E.; Zhao, Z.; Plessow, P. N.; Jelic, J.; Detlefs, B.; Pruessmann, T.; Studt, F.; Grunwaldt, J.-D. Photothermal Catalysis over Nonplasmonic Pt/TiO_2 Studied by Operando HERFD-XANES, Resonant XES, and DRIFTS. *ACS Catal.* **2018**, *8*, 11398–11406.

Citation: *CCS Chem.* **2024**, Just Published. DOI: 10.31635/ccschem.024.202404469
Link to VoR: https://doi.org/10.31635/ccschem.024.202404469